Volume 310 01 June 2018 ISSN 0169-555X

ELSEVIER

GEOMORPHOLOGY

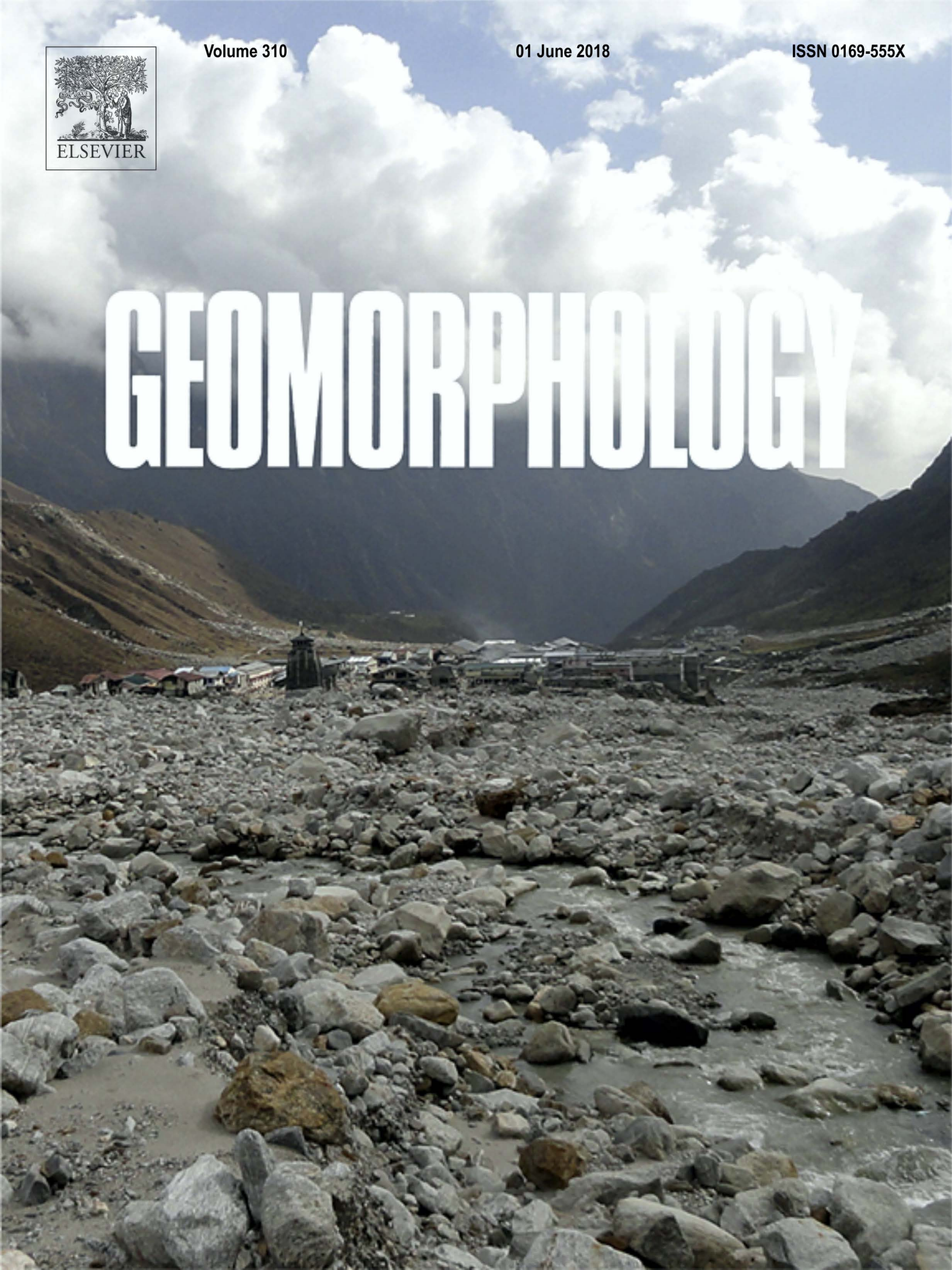

Volume 310 1 June 2018 ISSN: 0169-555X

ELSEVIER

GEOMORPHOLOGY

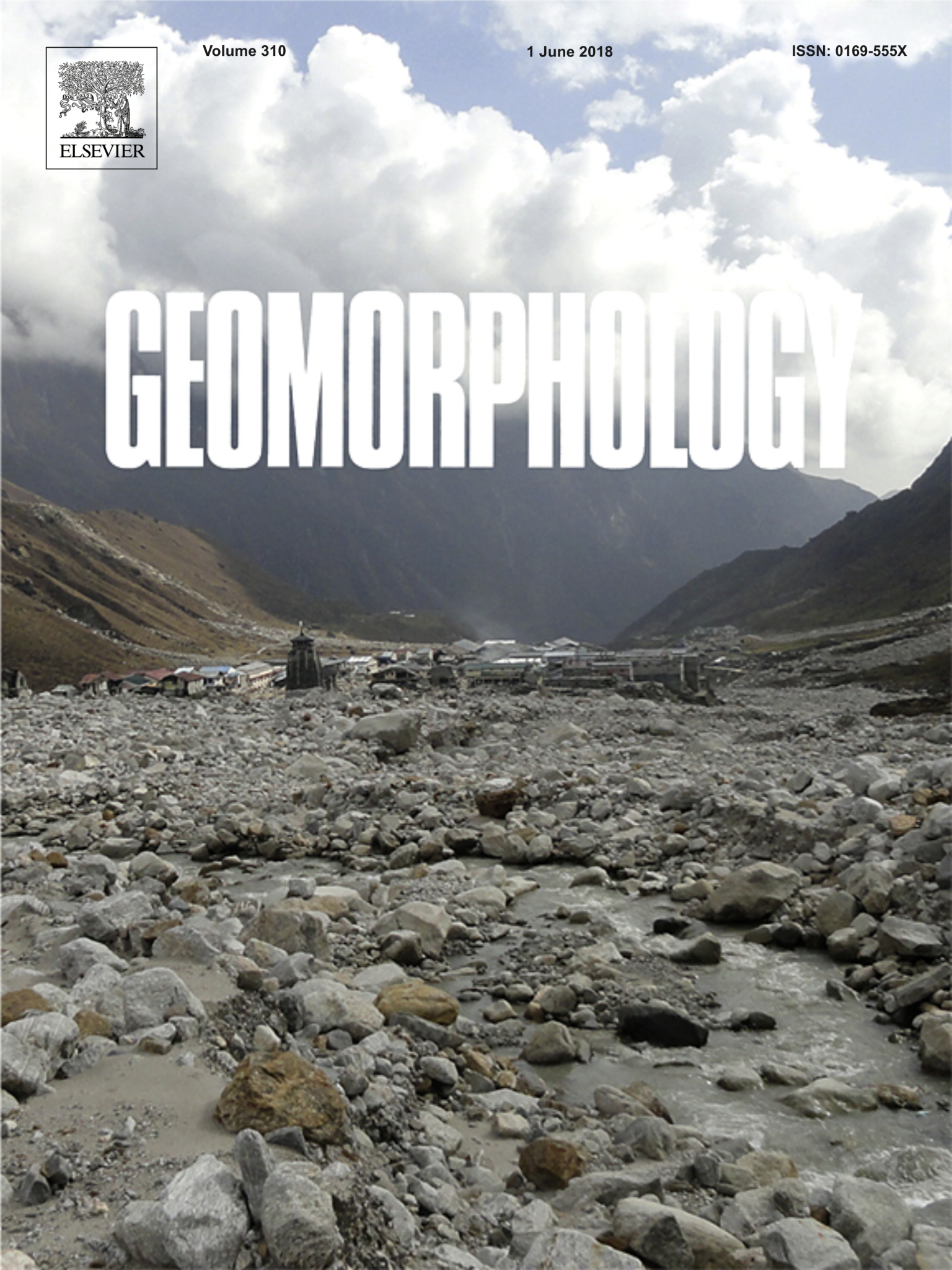

Geomorphology 310 (2018) 45–56

Contents lists available at ScienceDirect

Geomorphology

journal homepage: www.elsevier.com/locate/geomorph

ERT, GPR, InSAR, and tracer tests to characterize karst aquifer systems under urban areas: The case of Quebec City

Richard Martel [a], Pascal Castellazzi [a,b,*], Erwan Gloaguen [a], Luc Trépanier [a], Jaime Garfias [c]

[a] Institut National de la Recherche Scientifique (INRS), Centre Eau, Terre et Environnement, Université du Québec, 490 rue de la Couronne, Québec, QC G1K 9A9, Canada
[b] Commonwealth Science and Industrial Research Organisation (CSIRO), Land and Water, Waite Rd, Urrbrae SA 5064, Australia
[c] Universidad Autónoma del Estado de México (UAEM), Centro Interamericano de Recursos del Agua, Carretera Toluca-Atlacomulco, km 14.5. Ciudad Universitaria, C.P.50110 Toluca, Estado de México, Mexico

ARTICLE INFO

Article history:
Received 28 October 2017
Received in revised form 5 March 2018
Accepted 5 March 2018
Available online 06 March 2018

Keywords:
Karst
Sinkhole
Urban area
Multidisciplinary approach

ABSTRACT

Urban infrastructures built over karst settings may be at risk of collapse due to hydro-chemical erosion of underlying rock structures. In such settings, mapping cave networks and monitoring ground stability is important to assure civil safety and guide future infrastructure development decisions. However, no technique can directly and comprehensively map these hydrogeological features and monitor their stability. The most reliable method to map a cave network is through speleological exploration, which is not always possible due to restrictions, narrow corridors/passages, or high water levels. Borehole drilling is expensive and is often only performed where the presence of karsts is suggested by other techniques. Numerous indirect and cost-effective methods exist to map a karst flow system, such as geophysics, geodesy, and tracer tests. This paper presents the outcomes from a challenging application in Quebec City, Canada, where a multidisciplinary approach was designed to better understand the groundwater dynamics and cave paths.

Two tracer tests in groundwater flowing through the cave system indicated that water flows along an approximately straight path from the sinking stream to the spring. It also suggests the presence of a parallel flow path close to the one already partially mapped. This observation was confirmed by combining Ground Penetrating Radar (GPR) and Electrical Resistivity Tomography (ERT) techniques, and ultimately by observing voids in several boreholes drilled close to the main cave path. Lowering the water levels at the suspected infiltration zone and inside the karst, the infiltration cracks were identified and the hydraulic link between them was confirmed. In fact, almost no infiltration occurs into the karst system when the water level at the sinking stream drops below a threshold level. Finally, SAR interferometry (InSAR) using RADARSAT-2 images detected movements on few buildings located over a backfilled sinkhole intercepted by the karst system and confirmed the stability of the rest of the karst area. The knowledge of the flow system described in this paper is used by policy makers to assure civil security of this densely populated area.

1. Introduction

Karst aquifer systems are present throughout the world and represent 10% to 20% of Earth's surface area (Ford and Williams, 2013). Their large distribution ensures that they are regularly found under urban settings. The construction of infrastructure above karst aquifer systems, where voids frequently occur, poses major issues for civil engineering and public safety (Beck, 1984, 2002; Waltham et al., 2005; Del Prete et al., 2010). Such aquifers often have complex structures limiting their characterization. The development of voids and preferential groundwater flow paths follow various controlling factors and is difficult to predict (Chalikakis et al., 2011). No singular approach exists to map, understand, and monitor the behavior of karst systems because of their varying water saturation, depth, and shape. Consequently, complex and multidisciplinary studies involving a combination of techniques are often required to assess the associated risks to urban infrastructure.

In urban settings, geophysical methods such as seismic reflection, Electrical Resistivity Tomography (ERT) methods, and low-frequency Ground Penetrating Radar (GPR) work reasonably well (dos Reis Júnior et al., 2015). Satellite imagery interpretation by Interfrometric Synthetic Aperture Radar (InSAR) techniques are promising to detect infrastructure motion related to the erosion of underlying caves, as the abundance of hard and angular structures guarantee a high density of targets reflecting the emitted electromagnetic signal. Finally, groundwater tracer tests often

* Corresponding author at: Commonwealth Science and Industrial Research Organisation (CSIRO), Land and Water, Waite Rd, Urrbrae SA 5064, Australia.
E-mail addresses: Richard.Martel@ete.inrs.ca (R. Martel), Pascal.Castellazzi@ete.inrs.ca, Pascal.Castellazzi@csiro.au (P. Castellazzi), Erwan.Gloaguen@ete.inrs.ca (E. Gloaguen), Luc.Trepanier@ete.inrs.ca (L. Trépanier), jgarfiass@uaemex.mx (J. Garfias).

https://doi.org/10.1016/j.geomorph.2018.03.003
0169-555X/

reveal useful information regarding the groundwater flow path and dynamics.

Seismic reflection is based on the propagation of mechanical waves and specifically the body waves *P* and *S* into the ground. The method implies emitting elastic waves and monitoring their reflection over time with receivers (geophones) located at the surface. Several studies using seismic waves have helped detection of karst-related anomalies following the analysis of the propagation velocity of *P* and *S* waves (Belfer et al., 1998; Hoover, 2003; Parker, 2002). Recent developments in high-resolution seismic reflection have led to applications in urban areas (Krawczyk et al., 2013). For example, Di Fiore et al. (2013) presented its use to detect caves in Italy.

Electrical Resistivity Tomography (ERT) consists in emitting a DC current between two electrodes and measuring the difference of electric potential between two other electrodes (Roth et al., 1999; Rubin and Hubbard, 2005). The difference of electric potential *V* is interpreted using the relation between the intensity of the injected current *I*, the resistivity *R* of the ground (in Ohms), and *V*. Parameter *V* is influenced by the spatial distribution of electrical resistivity and electrode positioning at the surface. Inversion algorithms are used to assess the spatial distribution of resistivity in the ground that explains the measured electrical potential. Several types of inversions exist, and the most often used is the regularized least-squares method (Rubin and Hubbard, 2005). Ultimately, the method provides a two-dimensional section or profile of the ground resistivity and allows for the detection of anomalies such as voids which are extremely resistive.

Ground Penetrating Radar (GPR) is an ElectroMagnetic (EM) technique consisting of emitting an EM pulse into the ground within the radio frequency range (10–1000 MHz). A part of the signal is eventually back-reflected to a receiver antenna close to the emitting one when it encounters contrasts of electrical permittivity. Typically, the antenna pair is moved at the surface, and the reflected signal is constantly recorded. A measurement of EM wave intensity reflection in function of time and space is obtained. The conversion from time to depth is performed by fitting hyperbolas on the diffracted signal (Rubin and Hubbard, 2005). Typically, GPR surveys are performed along profiles. If multiple profiles are acquired in a spatially dense pattern, a 3D cube of GPR traces can be produced. It allows following the continuity of karstic channels when observed over multiple subsequent parallel 2D profiles. The technique is used by civil engineers to map underground structures. It is very sensitive to pipes and other shallow artefacts that may limit its depth of penetration and renders its interpretation complex in urban or highly heterogeneous environments.

Synthetic Aperture Radar interferometry (InSAR) is a fast-developing technique efficient to monitor ground movement (e.g., Castellazzi et al., 2016, 2017). It consists in interpreting the phase shifts between several identical EM wave signals (1–10 GHz) sent by a Synthetic Aperture Radar (SAR) satellite from the same orbital position and at different times (Massonnet and Feigl, 1998; Ferretti et al., 2001; Berardino et al., 2002). The phase shifts not related to ground motion are estimated and subtracted. Ultimately, ground displacement over time and along the satellite Line Of Sight (LOS) angle is inferred. On one hand, using InSAR as an early warning tool assumes the occurrence of precursory movements before collapse. On the other hand, identifying and mapping sinkhole collapse with InSAR is limited by our ability to convert the phase shifts into LOS distance change (solving 'the phase ambiguity') for sudden and nonlinear movements. Indeed, phase-to-displacement inversion algorithms usually rely on analysing the progressive component of phase shifts in time and/or space. In the case of sinkhole collapse, the phase difference is expected to be largely nonlinear in time and space (sudden movement over a limited area).

Despite its main limitations, several authors successfully used InSAR to detect karst-related ground movements or to observe the potential occurrence of precursory signs before collapse. Recent studies demonstrated the utility of InSAR for sinkhole detection and monitoring in natural settings (Gutiérrez et al., 2011; Atzori et al., 2015; Galve et al., 2015), in mining environments (Rucker et al., 2013), and in urban/built environments (Yerro et al., 2014). Intrieri et al. (2015) successfully used Ground-Based InSAR (GB-InSAR, which uses the same principle as InSAR on a fixed ground-based system) for early-warning of sinkhole collapse in Italy, pointing out the remaining potential offered by space-borne InSAR toward such applications.

Groundwater tracing techniques consist in adding a given mass of a traceable substance at the sinking stream and monitoring its arrival at one or several downstream springs or flow conduits. The transport times and the tracer mass balance are used to infer the occurrence of active conduits, their water flow rates, and the hydrodynamic links between the sinking stream and the springs. Kass and Behrens (1998) and Goldscheider et al. (2008) provide a complete description of the available tracers, their related applications, and the advantages and drawbacks of each. Among them, salts (which dissolve into cations and anions) and fluorescent dyes are the most used. The latter has the advantage of being visually observable and precisely quantifiable on site and in real time.

Recently, several authors performed case studies illustrating the value of combining techniques in order to improve the understanding of these complex aquifer systems. In a case study in Spain, Carbonel et al. (2014) described a multidisciplinary approach that includes a stereoscopic interpretation of aerial photos, the creation of a Digital Elevation Model (DEM) from a LIght Detection And Ranging (LIDAR) survey, a combination of GPR and ERT, InSAR, and linear excavations (exploration trenches). The authors note the importance of the geomorphological model to help with field work planning and result interpretations and to propose adapted risk mitigation measures. Lollino et al. (2015) suggested the following workflow to map and monitor caves: map geological features and define stratigraphy, interpret aerial photos and perform SAR interferometry (InSAR), drill boreholes, apply the available geophysical methods (including pilot tests to identify the right techniques), analyze water level variations, map hydraulic conductivity, estimate groundwater flow rate and direction, and identify recharge (sinking stream) and discharge (springs) areas. In another case study in Italy, Zini et al. (2015) used vertical borehole data, geotechnical surveys, GPR and seismic reflection, and hydrogeological and geochemical field investigations. They conclude that the multidisciplinary approach was essential to produce a reliable hydrogeological model, which was impossible using one method alone. Galvão et al. (2015) classified a karst system into five zones of risk according to the geological and hydrological conditions. The classification was based upon the analysis of aerial photos, the lithological profiles from boreholes, the optical inspection of boreholes with downhole camera, and a geological map.

The approach proposed in this study is inspired by previous multidisciplinary works (Cooper and Calow, 1998; Carbonel et al., 2014; Lollino et al., 2015; Zini et al., 2015) and involves a selection of techniques relevant in urban settings. It includes InSAR to detect ground movement, seismic reflection, a combined GPR/ERT survey to detect voids and cave, the drilling of boreholes on anomalies detected through geophysical methods, a hydrodynamic test with field monitoring of water level changes at the inflow/outflow of the system and inside the caves, and groundwater tracer tests to assess the spatial hydrodynamics of the aquifer system.

2. Study area

In spring 2013, a sinkhole appeared in the backyard of an apartment building in Quebec City, Canada, leading to the evacuation of four neighbouring buildings. Some of them showed signs of past ground movements, such as cracks on walls. The instability occurred over a ~6-m-thick and heterogeneous sediment backfill. Sediments were used there to fill a ~100-m-wide hole that appeared by collapse of a void created by hydrochemical erosion within the karst system and/or by the exploitation of a quarry (the history of the site is not entirely known). We assumed that the saturated portion of the backfill erodes

with groundwater flow. This paper presents a scientific approach designed to better characterize and understand the underground environment of this karst flow system.

The study area is located in the eastern part of the city, 8 km northeast of the center, and close to one of the most iconic tourist attractions: the Montmorency Falls. It extends on a surface area of ~0.4 km^2. The topography presents a slow slope with an elevation varying from 120 m to 80 m over 1 km. Caves are located in horizontally layered fine grain limestone with interbedded calcareous shale (finely laminated calcilutite) of the Neuville Formation. Carbonates and shales have similar aqueous dissolution rates when in contact with groundwater (Martel et al., 2016), so horizontal shale beds do not control the karst geometry. The potential karst zone is at least 23-m-thick where Precambrian metamorphic gneiss acts as the lower boundary. The caves have the same orientation as joints and fractures observed on local outcrops suggesting that they develop preferentially along these existing geological patterns.

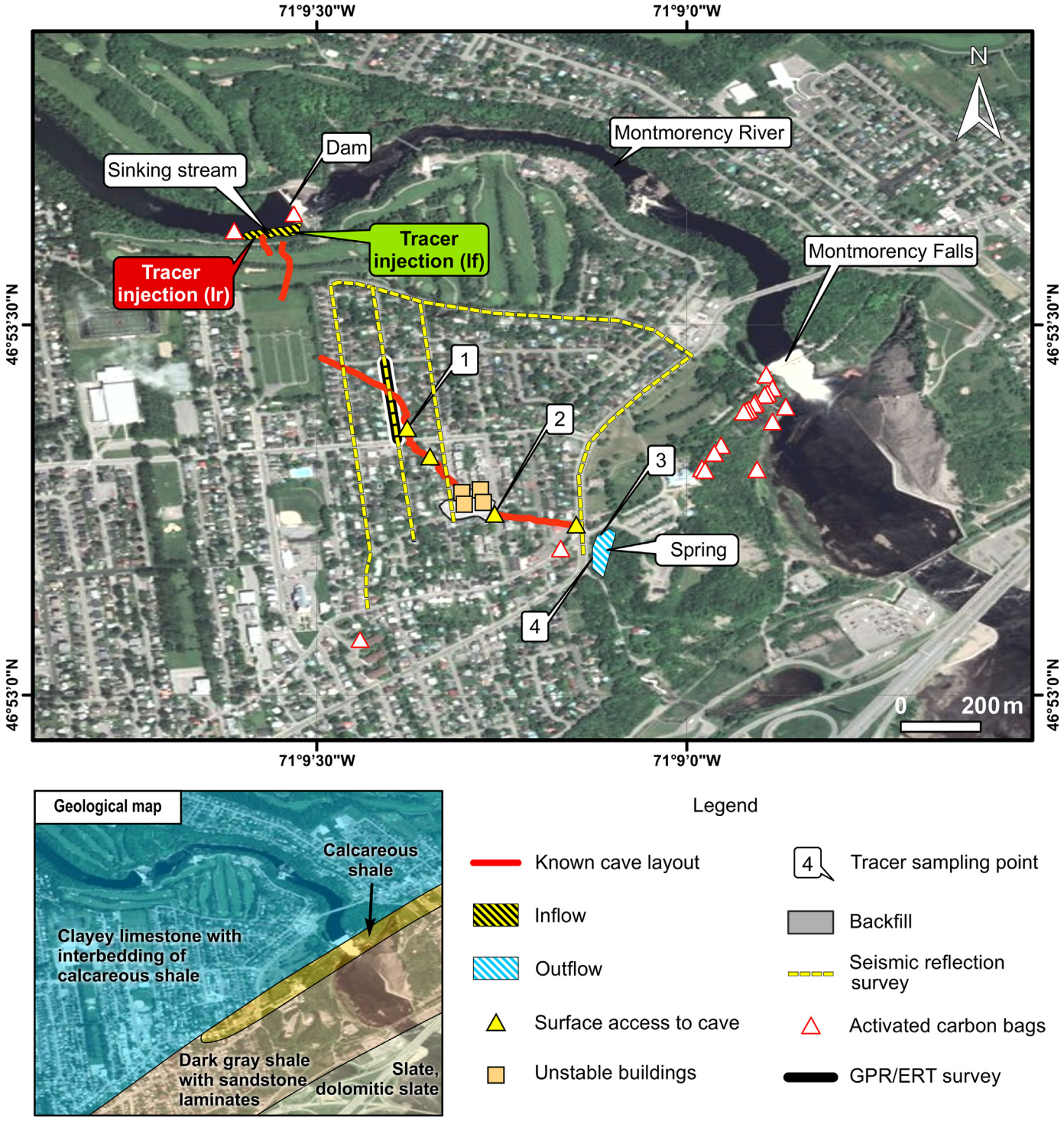

Fig. 1. Presentation of the study area, main landmarks, and data acquisition. Points 1, 2, 3, and 4 are accessible sampling locations used for the tracer tests. Geology from SIGEOM web map service: sigeom.mines.gouv.qc.ca.
Base map sources: ESRI, DigitalGlobe, Earthstar Geographics, CNES/Airbus DS, USDA, USGS, AeroGRID, IGN, and the GIS User Community.

We assumed that these conduits are enlarged via dissolution and hydromechanical erosion. Up to 3 m of heterogeneous surficial deposits with grain size ranging from clay to gravel covers the carbonate bedrock.

In the accessible sections of the caves, vertical fractures ~0.5–1-m-wide and up to ~10-m-high occur (Speltech, 2013a, 2013b, 2014). The ceiling thickness varies from ~0.5 to ~3 m and is made of flat-lying limestone or breccia. The caves are fed with water from the Montmorency River through open fractures in the carbonate bedrock along 200 m on the riverbank (Figs. 1 and 2). Based on geochemistry data (comparing major ion concentrations of the Montmorency River and the water flowing out of the cave), we estimated that 98.4% of the water at the springs area comes from the Montmorency River (Martel et al., 2016). The total vertical charge loss between the infiltrations into the karst system at the dam and the outflow at the spring is ~26 m. The cave's length is about 980 m long, which suggests an average hydraulic gradient of 2.7%. The water level at the river is usually maintained above the infiltration fractures by a run-of-river hydroelectric dam. The average flow rate at the spring area is ~1 m^3/s.

3. Material and methods

3.1. Hydrodynamics

A hydrodynamic test was conducted to verify the links between the caves and the dam along the Montmorency River. The test consisted of lowering and recovering the water level at the dam to change the hydraulic head over potential infiltrating fractures located on its banks. The flow rate was monitored downstream of the karst system 37 times during the test, which occurred between 18 and 22 August 2015. The outflow rate was estimated at two locations (3 and 4 on Fig. 1) to cover the entire cave system outflow. The spring flow rate was measured using a velocimeter at location 3 (Marsh-McBirney Flo-Mate 2000; Marsh-McBirney Inc., 1994). The tracer dilution test method (Rantz, 1982; Moore, 2005) was used in location 4 as the flow was largely nonlaminar. For such tests, a brine solution was injected at one point, and the electrical conductivity was monitored 150 m downstream with three probes at 1/3, 1/2, and 2/3 along a transect perpendicular to the flow.

3.2. Dye tracing

Dye tracer tests were conducted on 9 October 2013 with the objective of better understanding the groundwater dynamics and flow path. Fluorescein and Rhodamine WT were injected simultaneously in two infiltration holes (If and Ir respectively) at the upstream section of the karst system, along the Montmorency River shoreline (Fig. 1). The two tracers were chosen because of their very low reactivity with carbonate rocks (Davis et al., 1985). The fluorescein and rhodamine WT solutions were obtained by adding 410 g of tracer into 20 L of water. The solutions were stored at 4 °C in light-proof containers before injection. Water samples were collected simultaneously at four locations downstream. Two sites are located in the cave along the flow path at 520 m (see 1 on Fig. 1) and 770 m (2) from the injection points. Two other sampling sites (locations 3 and 4) are located at the main discharge area (980 m from the injection points). The water flow rates were measured at each location with the velocimeter method.

Water samples were taken every 10 min at the beginning, then every 2 min when the tracer concentration was visibly high, and finally every 5 min at the end of the test. The last sample was taken around 4 h after the injection. The samples were collected in vials and immediately stored at 4 °C. They were analysed using a Varian Cary Eclipse Spectrofluorometer. Excitation/emission wavelengths were set at 490/512 and 564/582 nm for fluorescein and rhodamine WT, respectively.

In addition to the tracer test, two activated carbon bags were positioned upstream and downstream in the Montmorency River and tested to assure that tracer solutions entirely infiltrated into the karst system. Activated carbon bags were also placed in other springs across the area (Fig. 1) to verify their connection to the cave system. Their use followed the method described by Aley (2002). To assess the dye tracer mass balance, flow rate was measured at every tracing location using a velocimeter (Marsh-McBirney Flo-Mate 2000; Marsh-McBirney Inc., 1994).

3.3. Seismic reflection

A seismic reflection survey on streets of the karst area sector was performed in October 2013 by MBMS Solution Inc. (Fig. 1). The seismic source is a sweep with frequency ranges between 20 and 500 Hz, and a streamer of 48 geophones having a spacing of 0.75 m was pulled by a

Fig. 2. Example of an infiltration hole along the Montmorency River bank at the dam observable after decreasing the water level (left picture; see inflow location on Fig. 1) and view inside an accessible section of a cave (see point 2 on Fig. 1).

truck. The survey was carried out over a length of 3.2 km at night to minimize noise bias. Data were processed with Seismic Unix software (Stockwell, 1999) and in-house MBMS Solution Inc. algorithms.

3.4. GPR and ERT

The GPR and ERT surveys were performed assuming that the karst system largely included water-free voids. In this context, techniques able to map resistivity (ERT) and permittivity (GPR) contrasts in the ground are promising. The GPR is a high resolution technique that maps interfaces between materials by detecting contrasts of electrical permittivity in the top 5-10 meters depending on the antenna frequency and the ground electrical properties. On the other hand, ERT has a lower resolution, and the in-depth distribution of electrical conductivity is inferred by inversion. The latter is less sensitive than GPR to shallow human infrastructure such as pipes or cables. In this paper, the 3D GPR cube and the 2D ERT profiles acquired along the same road are combined and interpreted together in order to take advantage of both methods. The survey was performed at a pilot scale, it consisted of >200 m of GPR traces and ~96 m of ERT lines. The survey crosses a portion of the known cave path (Fig. 1).

Ten parallel GPR profiles were acquired along Sylvio Street (Fig. 1) in the perspective of mapping the underlying open fractures. The GPR system used an antenna frequency of 100 MHz (from Mala Geoscience) with a GPS time sampling interval of 0.5 s (i.e., every ~20 cm). The acquired raw GPR data consists of reflected, diffracted, and refracted EM waves (in micro V) as a function of time. The processing applied to the data consists in a low frequency correction (dewow), a static correction, an automatic gain compensation, and a band-pass filtering. The 10 profiles were interpolated on time slices and aggregated in a 3D cube. Finally, a time-to-depth conversion was computed with a velocity of 0,09 m/ns. This velocity was estimated by fitting hyperbolas on diffractors.

One ERT profile was taken along the east side of Sylvio Street with a SYSCAL Pro (IRIS Instruments). The ERT required the drilling of 96 20-cm-deep holes into the road (i.e., every meter; Fig. 3). The ERT survey was done with a dipole-dipole configuration that allows for a better lateral resolution. The acquired raw ERT data consist in approximatively 5000 measured electrical potential. The processing consists in removing outliers, check reciprocity, and inverting for the electrical potential. It was computed using Res2dInv software. Finally, a 2D vertical section of the ground resistivity along the electrodes path was obtained. Conventional Marquardt-Levenberg inversion was used, and the damping factor was adjusted using the L-curve method (Tarantola, 1984).

3.5. Drilling

Boreholes were drilled in winter 2015 along the path of the geophysical survey (Fig. 1) in order to validate the results. A total of eight subvertical boreholes (15° from the vertical), ranging from 10.9 to 17.4 m deep, were drilled with a diamond drill rig. The bedrock formation was sampled with an NQ corer and water losses during drilling were recorded in drill logs. Borehole locations are illustrated along with the results from the geophysical survey in Fig. 10A.

3.6. InSAR

The SAR images are processed to measure movements of urban infrastructure. The Persistent Scatterer Interferometry (PSI) algorithm based on Ferretti et al. (2001) and implemented into SARScape® 5.2 (http://www.sarmap.ch/) was used to process 35 Ultrafine (U6; MDA, 2016) RADARSAT-2 images acquired over the study area from 29 March 2008 to 1 September 2015. All images are coregistered and compared with a central master (Fig. 4).

The PSI processing consists in identifying the best ground targets in terms of signal amplitude and coherence stability over a stack of SAR images. Once the ground targets are identified, the phase variation over time unrelated to ground displacement is estimated and subtracted. Using a linear deformation model, the remaining phase variations are inverted into displacement time series for every ground target. Compared to other InSAR processing strategies, PSI is particularly suited for this study as it allows producing high resolution ground displacement maps in urban areas, where coherent scattering targets are dense. A detailed explanation of the different PSI processing strategies is provided by Crosetto et al. (2016).

Fig. 3. ERT measurements in the field (Fig. 1).

4. Results

4.1. Hydrodynamics

Fig. 5 shows the relationship between the water level upstream of the Montmorency River dam and the water flow rate at the spring. The outflow from the caves (blue curve 1, Fig. 5) decreased from 0.930 to 0.020 m^3/s, which represents a 98% flow rate loss when the water level in the river dropped 1.5 m below its normal level (112.25 m asl). The flow rate downstream of the karst system stabilized even if the river level kept decreasing below 111.75 m asl. It means that the fractures from which water infiltrates into the karst system act as a level threshold below which water almost stops infiltrating. When the water level in the river is recovering (red curve 2, Fig. 5), the same threshold level can be observed. The gap between the red and the blue curves is related to the ~60-min transit time between the springs and the dam.

This field test proves the direct hydraulic link existing between water level at the dam and the flow rate within the karst system. Therefore, lowering the water level upstream of the dam below 111.75 m asl or plugging the fractured bedrock along the river bank may result in a significant flow rate reduction. This may decrease the erosion under

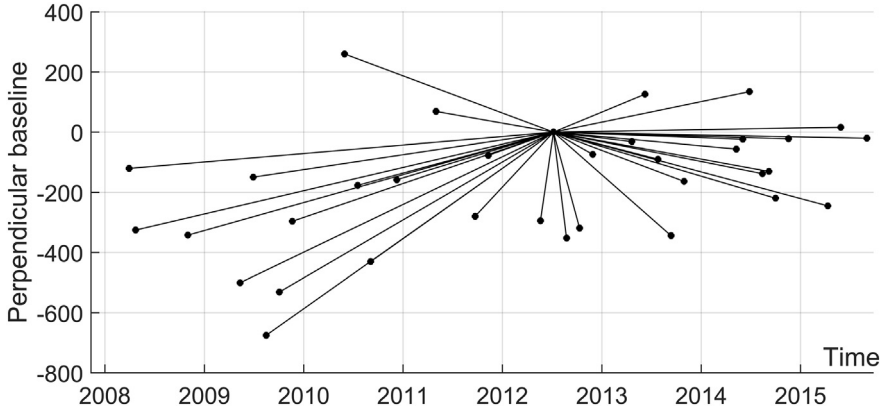

Fig. 4. Star connection graph used to link all SAR images of the RADARSAT-2 time series. Each connection represents an interferogram (a phase difference map) taken into account to retrieve the SAR phase variation over time for each highly coherent ground target (such as buildings).

the unstable buildings that were evacuated in spring 2013. In summer 2016, the Quebec City council decided to plug the infiltration holes at the dam in hope of stopping the subsidence in the backfill areas downstream.

4.2. Dye tracing

The activated carbon bags installed in the surrounding springs (Fig. 1) did not capture any dye tracer. This confirms that only springs at locations 3 and 4 are connected with the tracer injection sites Ir and If.

The dye tracer test was performed during a field campaign illustrated in Fig. 6. Fig. 7 presents the evolution of the fluorescein and rhodamine WT concentrations at four sampling points (1 to 4), starting from the dye injection. Two locations are within the cave system (1 and 2) and two others are at the springs (3 and 4). Results show that sites located farther from the injection points have lower maximum concentrations and smoother breakthrough curves, which is caused by mechanical dispersion and molecular dilution. The shape of the breakthrough curves at points 3 and 4 suggests that water infiltrating into the cave system from the Montmorency River bank follows either a single trajectory or several trajectories of ± similar lengths. Indeed, if part of the water had followed a path with a significant length difference, the time vs. concentration curves would have presented several concentration peaks (multimodal shape).

The time corresponding to the maximum dye tracer concentration of each curve in Fig. 5 represents the transit time from the injection point to the sampling position. For all sampling locations, the fluorescein concentration peaks always arrived before the rhodamine WT peaks. Fluorescein is considered as a truly conservative tracer (Aley, 2002), whereas rhodamine WT may be delayed because of its adsorption over inorganic surfaces (Aley, 2002). For this reason, using the fluorescein concentrations over time is recommended to infer water transit times.

The fluorescein and rhodamine WT transit times are reported in Fig. 8 and related to straight-line distances from the injection point. It took respectively 48, 69, and 83 min for fluorescein to arrive at locations 1, 2 and 4 located 520, 770, and 980 m away from the injection point (If – Fig. 1). The points in Fig. 8 are aligned, indicating that the flow path into the cave follows ± a straight line from the injection point to the sampling points. The average water velocity is 0.19 m/s (corresponding to 11 m/min).

A mass balance of dye tracers was calculated for each sampling location by multiplying the measured concentrations by the water volume flowing between each sampling intervals (i.e., obtained by multiplying the flow rate by the time period between sampling events). Fig. 9 shows that fluorescein arrived in location 1 first, then in location 2, and finally at the springs (3 and 4). More importantly, the mass balance indicates that only 24% (98 g/411 g) and 66% (271 g/411 g) of the fluorescein mass transits within the known cave at locations 1 and 2 respectively. It also shows that the tracer mass is entirely recovered at the downstream sampling locations (3 and 4 In Fig. 1). This reveals the presence of one or multiple water flow paths (and possibly caves) different from the known one. Even though it does not provide information about the size and shape of the other flow paths, the mono-modal shape of the breakthrough curves (Fig. 7) suggests that the alternative flow paths are close to the known one.

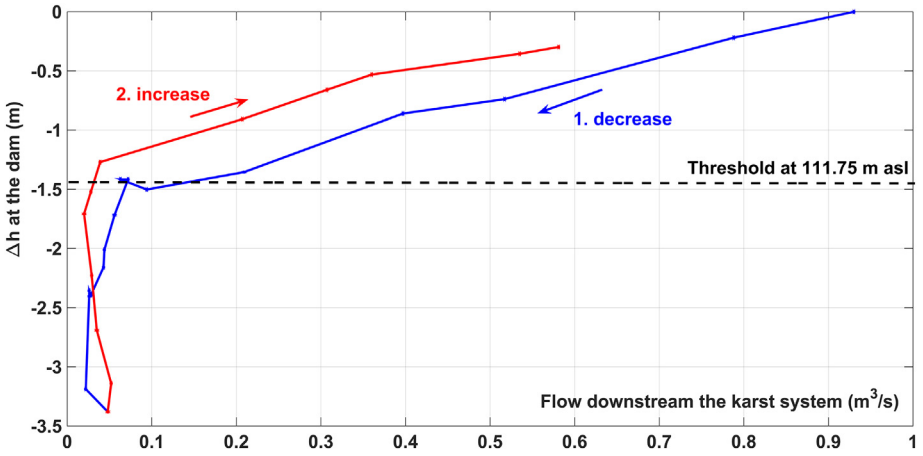

Fig. 5. Results from the hydrodynamic test. The water level in the dam was decreased in order to confirm its hydraulic link with groundwater within the karst system. A groundwater-fed base flow of 0.02 m^3/s is observed when the water level in the upstream river is below the infiltration threshold of 111.75 masl.

Fig. 6. Water sampling in an accessible cave during the fluorescein dye tracer test (top – site 1 on Fig. 1) and at a spring (bottom - site 4 on Fig. 1).
(Top picture by Guillaume Pelletier.)

The overestimation of the fluorescein mass at the outflow area, locations 3 plus 4, (138%, 568 g/411 g) is attributed to the imprecision of the water flow measurements. Indeed, finding a place respecting the laminar flow condition imposed by the velocimeter method was not always possible. This caused important uncertainty when measuring the water velocity at location 4.

4.3. Seismic reflection

Analysis of the seismic results indicated that no clear seismic attribute could guide the interpretation and infer the presence of karst. The inability to reach a robust interpretation from these measurements was related to: (i) the thin sediment layer above the bedrock transition that results in a rapid change in seismic velocity and apparent reverberation; (ii) the presence of infrastructure providing an equivalent seismic response (attenuation) to the one produced by the caves; (iii) the excessive speed of propagation of seismic waves in bedrock and the rapid attenuation of high frequencies that reduces the resolution of the method and prevents the detection of narrow caves; and (iv) the shallow depth of the caves, which leads to a superposition between the surface waves and the expected reflection response of the shear waves. This method was therefore not recommended for further investigation in the study area.

4.4. GPR and ERT

The combined interpretation of GPR and ERT was aimed at identifying qualitative targets for drilling sites in order to confirm the cave path. Fig. 10 shows four depth slices (at 0.6, 4.0, 6.2, and 10.8 m) selected within the 3D GPR cube and the corresponding 2D ERT profile. The ERT profile has a poor spatial resolution, and the depths of the anomalies are expected to be imprecise. On one hand, most of the ERT profiles show conductive zones (in blue) that are probably nonkarstic. Indeed, one of the main objectives of the technique is to discard zones where a borehole-based karst exploration is not required. On the other hand, the ERT profile shows three very strong resistive anomalies (A, B, C in red/orange) correlated with some deep anomalies on the GPR slices (E and J). The ERT anomaly C corresponds to GPR anomaly J (10.8 m) and to a known section of the cave, whereas the ERT anomalies A and B correspond to GPR anomaly E at (4.0 m). Two groups of anomalies located north (D, G, I) and south (F, H, K) are also visible on GPR slices (4.0, 6.2, 10.8 m) but are not covered by the ERT survey. These groups of GPR anomalies look similar to E and J and were identified as potential targets for drillings. This is particularly true for the southern anomalies (F, H, and K) that have the elongated shape typical for karstic channels. The first depth slice (0.6 m) on the GPR shows the strong influence of anthropic structures (e.g., pipes) and the change in bitumen starting from the third lower part (Fig. 10A: left side of the GPR model slice). These are not related to karstic voids.

The GPR/ERT combination is able to identify the known cave that confirms the efficiency of such combination and give confidence in results beyond the known area. In order to further map the cave system, we recommended making parallel ERT lines, producing a 3D map of anomalies, and improving the spatial resolution. All geophysical surveys should be oriented perpendicular to the known or expected cave direction to increase chances of interception.

4.5. Drilling

Borehole locations were decided upon the presence of geophysical anomalies and the known cave path (Fig. 10A). The drilling campaign indicated that the top of the limestone formation is from 1.4 to 3.6 m below the soil surface. The borehole logs are interpreted in relationship to the ERT and GPR geophysical measurements, as they aimed to provide validation.

Boreholes F1 and F2 — located north of the study area — are outside the limit of the ERT profile but are inside the GPR anomalies D, G, and I (Fig. 10). Voids of 0.1 and 0.5 m are found at 6.1 and 11.8 m respectively

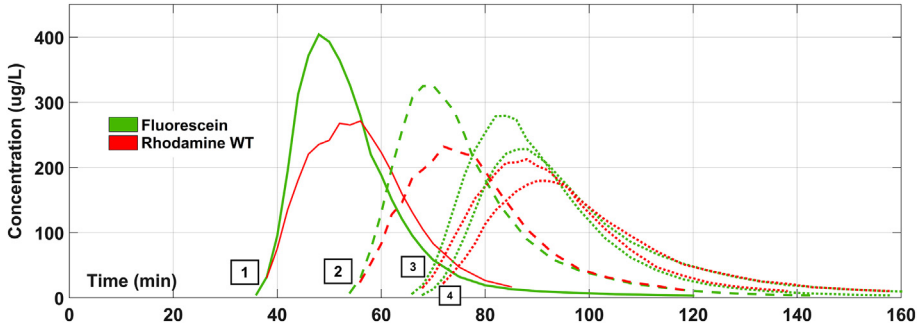

Fig. 7. Arrival of the tracer at the four sampling locations as shown in Fig. 1.

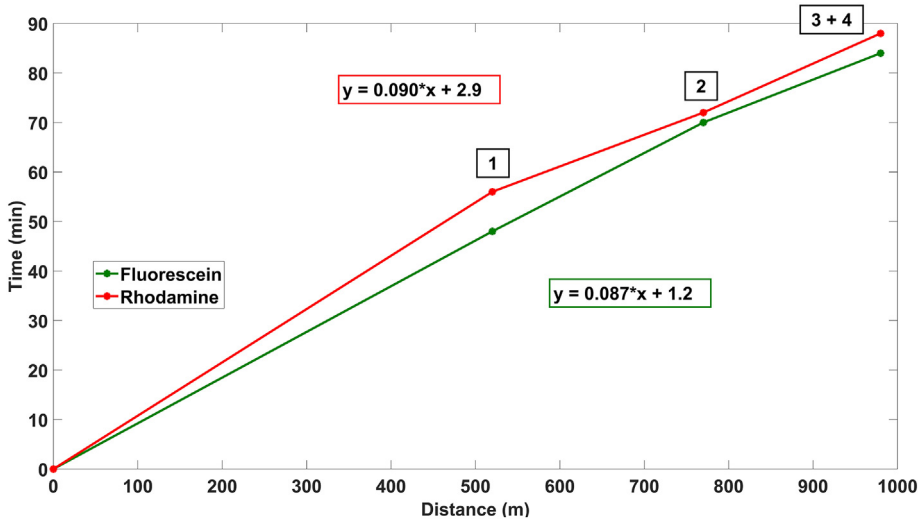

Fig. 8. Travel time of the tracers. The arrival of the concentration peak at every sampling location is related to the distance between the sampling locations and the injection point. Water travel time is constant and estimated between 0.087 and 0.090 min/m (corresponding to 0.19 m/s or 11 m/min).

in F1, corroborating the GPR anomaly. It may correspond to the ERT anomaly A extending in that direction as it corresponds with the direction of the known cave system. Fractured rocks (but no major voids) are found in F2. Borehole F1, GPR anomalies D, G, I, and ERT anomaly A suggest that a parallel cave path exists close to the main one. This confirms the conclusions drawn from the groundwater tracer tests about the occurrence of a secondary water flow path close to the known one.

Boreholes F3, F4, and F5 — located in the middle of the investigated zone — are above ERT anomaly C and above GPR anomaly J (for F3 and F4). Water losses were observed during drilling from 12.2 to 15.6 m in F3, voids from 7.2 to 7.3 m and from 9.0 to 10.9 m were detected in F4, and a void from 14.4 to 15.5 m was observed in F5. The anomaly identified at 10.8 m with the GPR (anomaly J) and ERT (anomaly C) was confirmed by drilling as a void of 1.9 m located between 9.0 and 10.9 m deep was found in F4. The 1.5-m-long void observed in F5 between 16 and 17.5 m depth is deeper than the deepest GPR slice but could correspond to anomaly C extending deeper in that direction. Observations during drilling and detected anomalies at these sites correspond well with the known presence of a cave.

Boreholes F6, F7 and F8 — located south of the investigated zone — are outside the limit of the ERT profile but are over GPR anomalies F, H and K. Fractured rocks were observed in those three boreholes, and drilling water losses were observed in F7 from 3.3 to 17.5 m even though no large voids were found.

Drilling confirmed the value of the combined ERT/GPR. Indeed, voids were found in boreholes where anomalies are simultaneously found by both GPR and ERT. Borehole drilling also confirms the existence of a parallel cave path along the known one, an assumption that was concluded following tracer test interpretation. The accessible caves in the area are narrow and high. In order to increase the chance of intercepting the cave, we recommend to drill confirmation boreholes toward the center of the GPR/ERT anomalies at a 45° angle from the vertical and perpendicularly to the cave orientation.

4.6. InSAR

Results of InSAR processing are presented in Fig. 11. Green points correspond to stable targets showing vertical movement inferior to ± 2 mm/y. The regional map indicates that the Quebec City area is globally stable (Fig. 11A). The known cave path, backfill sinkhole, and PSI results are shown in Fig. 11B. The map indicates stable points (green) with sparsely distributed yellow points (movement of 2–3 mm/y). The

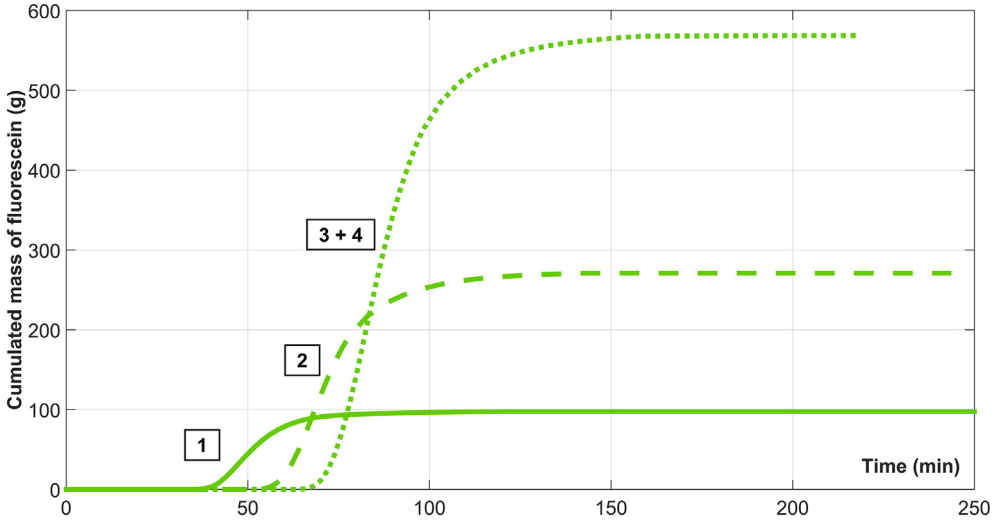

Fig. 9. Cumulative fluorescein mass at different locations, calculated from concentrations and water flow rates. The total mass injected was 410 g. Overestimation of the mass can be caused by imprecisions of the water flow rate measurements at location 4.

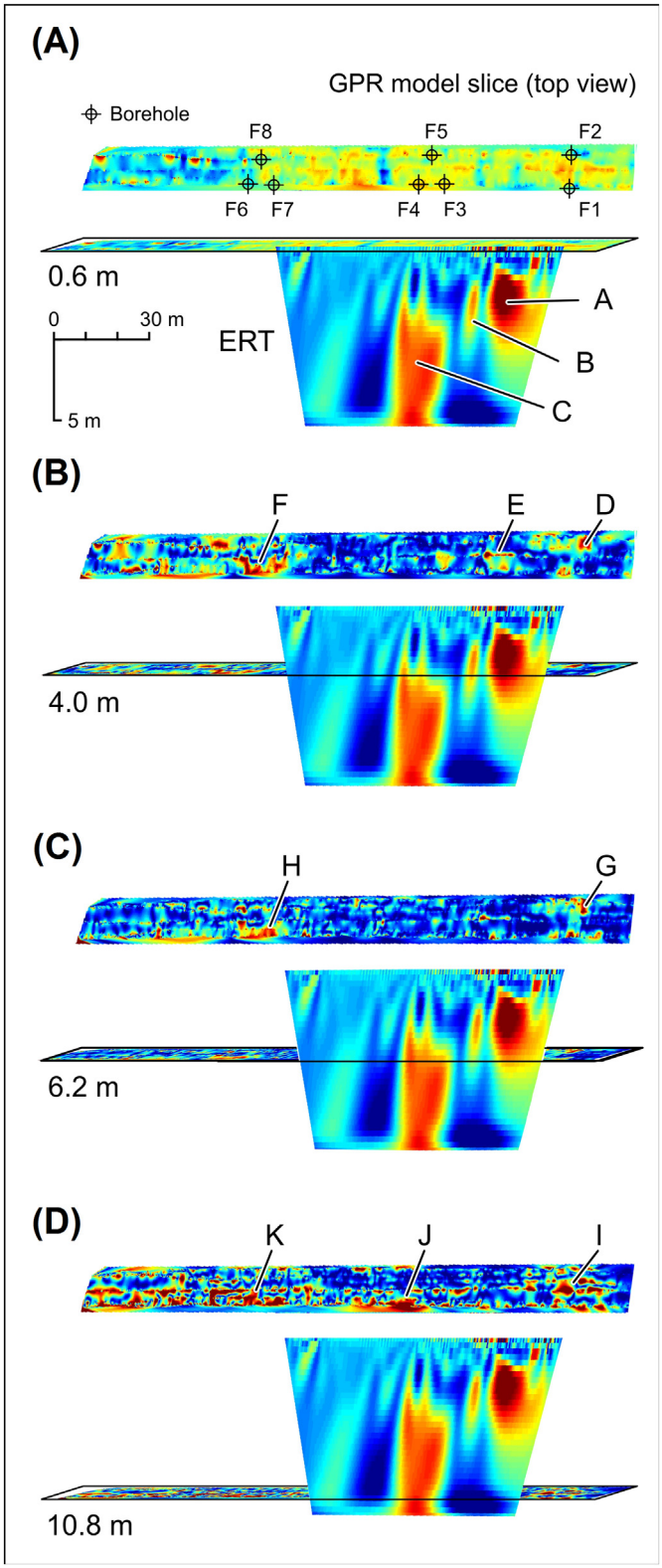

Fig. 10. Cointerpretation of results from GPR at four depths and ERT. The survey was designed to intercept the known cave path (see Fig. 1) and detect other possible caves close to the known one, as suggested by the tracer test. F1 to F8 are borehole locations, A–C are ERT anomalies, and G–I are GPR anomalies.

yellow points do not necessarily correspond to ground vertical movement if they are isolated, as they can also represent unstable SAR backscattering targets positioned on stable terrain (public lights, unstable walls, etc.). Confidence in the detection of unstable terrain increases as several adjacent points show coherent and temporally progressive movement. A zoom on the backfilled sinkhole/quarry (Fig. 11C) shows a cluster of yellow/red points (29075) that coincide with the backfill area where building instability occurred in 2013. Another cluster of yellow points (e.g., 26104 and 26806) is located on an unstable slope alongside the springs. It is not of concern as no major infrastructure is present in this area. No other unstable target cluster was identified along the possible cave path.

Displacement time series of several targets are shown in Fig. 12. The grey area represents the mean displacement ± one standard deviation of 1000 randomly selected points throughout the study area and is used to discriminate movements beyond the observable background noise. The six time series presented are all showing slow subsidence movement beyond the detection threshold (Fig. 12: curves and grey area). The displacement time series of several unstable points also suggests that phase offsets and sudden displacement occur (Fig. 12: peaks on curves 29,501 and 29,074). This is observed when the phase shifts over time do not match the deformation model they are fitted on. This can occur, e.g., when the terrain level or the structure of the ground target has changed suddenly (creating a phase shift that is not explainable by the deformation model).

As previously mentioned, a major limitation of the PSI method lies in discriminating terrain movement from target instability. A target can be unstable and installed on stable ground (e.g., an electrical post). Another limitation regarding the use of PSI is linked to the wrapped nature of the phase. As the study was partially motivated by building movements in spring 2013, spatially limited subsidence of amplitude above 14 mm ($\lambda/4$) between two acquisition dates is expected. Thus, the quantification of displacement rates may be compromised for these dates. Finally, detailed interpretation of the results in space (Fig. 11) and time (Fig. 12) should be taken with caution, given that all detected movements are close to the observed detection limit in spatial extent and in temporal signature.

Considering the inherent limitation of the technique, PSI still provides valuable information. Indeed, the InSAR-derived deformation map (Fig. 11C) shows the terrain stability over the expected cave path and instability in two well-defined and spatially limited areas. The PSI also provides a unique insight into the historical displacement when the required SAR archives are available. It also offers interesting perspectives toward the creation of early-warning systems adapted for sinkhole collapse. The occurrence of temporally progressive displacements prior to collapse have first to be confirmed and well characterized.

5. Conclusions

To obtain a better understanding of a karstic flow system under urban area, the approach should be multidisciplinary and should account for the inherent limitation of each method. In this paper, we combined hydrogeology with geodesy and geophysics.

Our approach starts with a quantitative tracer test to provide mass balance estimates and to assess groundwater transit times. This method is cost-effective, fast, and easy to implement as long as accessible points can be identified along the cave system. In this study, it led us to understand that: (i) the water flow path between the sinking streams and the springs follows a ± straight line (arrival times at the observation points are linear); (ii) water flows within other conduits than the known ones (tracer masses vary significantly along the path); (iii) the unknown cave path is probably close to the known one (as the tracer breakthrough curves are monomodal); and (iv) the water from sinking streams entirely exits at solely one spring area (the tracers were never detected in other springs or surface water bodies across the area).

The presence of urban infrastructure makes geophysical data interpretation complicated and, as such, not all methods work. This study showed the importance of making pilot tests with the selected geophysical methods over a known portion of the cave system. As a matter of fact, the seismic method failed, but the combination of GPR and ERT surveys

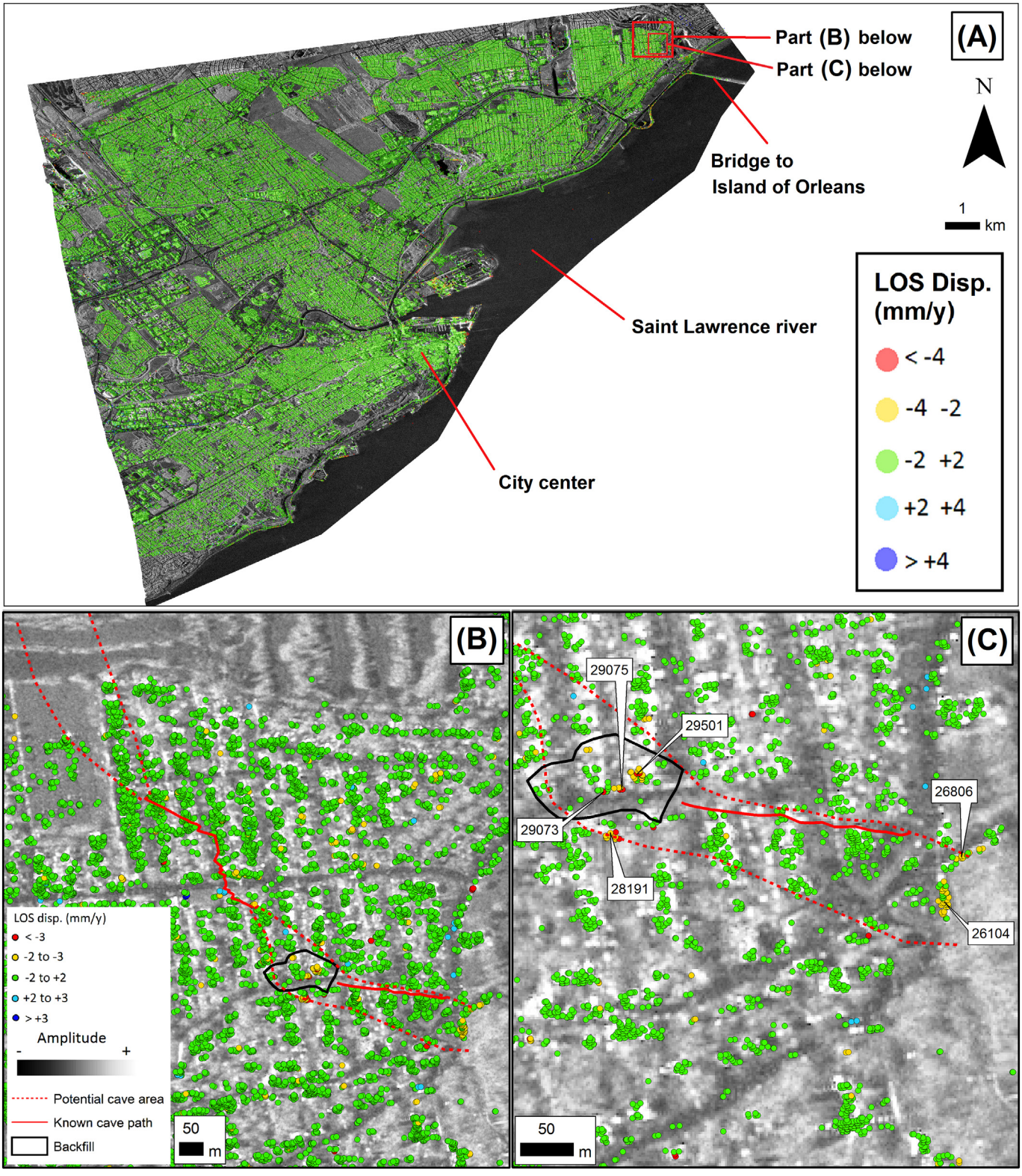

Fig. 11. Average vertical displacements from April 2008 to September 2015 measured by PSI: (A) Regional overview, (B) study area, and (C) close up on vertical movements over the karst area.

was able to identify three anomalies associated with voids likely contributing to groundwater flow within the karst system. Furthermore, ERT alone can be used to confirm the absence of karstic voids. Further investigations could focus on deploying the GPR/ERT combination over the entire study area and possibly intercept other voids. The survey design should take into account the state of knowledge regarding the karst orientation. At best, it is positioned perpendicular to the expected karstic features. Speleology and borehole drilling are the only methods that can be used to confirm with certainty the presence of caves.

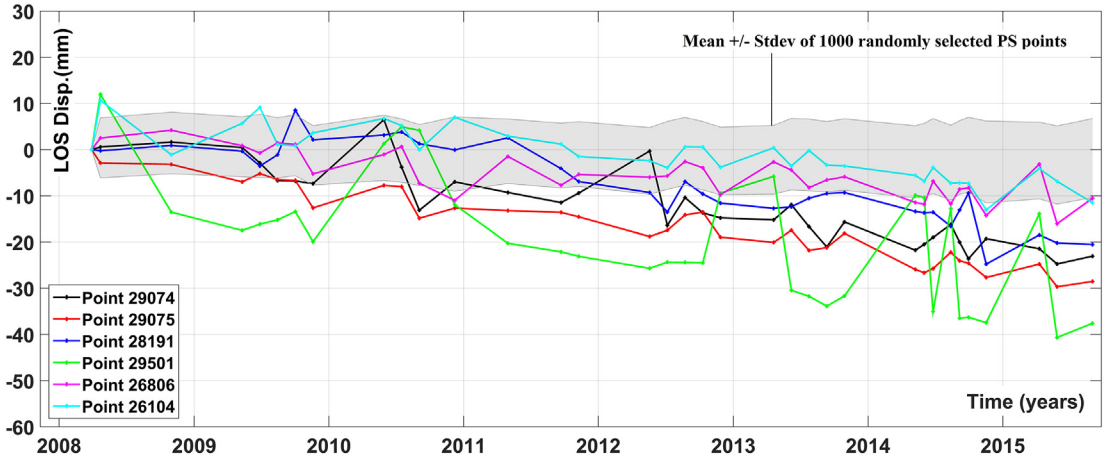

Fig. 12. LOS displacement time series of the PS points shown in Fig. 9.

Finally, archived SAR images analysed by the PSI algorithm can be used to determine the stability of a karst and to backtrack historical ground movements. The global coverage of the recent Sentinel-1 satellites assures SAR data acquisition from 2014, with a high temporal density, and over most karstic settings of the world.

Acknowledgements

This study was conjointly supported by the City of Quebec and by the Canadian Space Agency (CSA) through the Science and Operational Applications Research (SOAR) program, project # E-5334. The project was also funded by the NSERC discovery grant of Prof. Richard Martel (#RGPIN-2016-06503). The authors thank Marco Boutin, Clarisse Deschênes-Rancourt, Richard Levesque, Veronika Varfalvy, Angus Calderhead, Uta Gabriel from INRS-ETE, and Denis Lavoie from the Geological Survey of Canada. The authors also thank four anonymous reviewers and Richard A. Marston (Editor-in-Chief) for their help improving the manuscript.

References

Aley, T., 2002. The Ozark Underground Laboratory's Groundwater Tracing Handbook. Ozark underground laboratoy (36 pp).

Atzori, S., Baer, G., Antonioli, A., Salvi, S., 2015. InSAR-based modeling and analysis of sinkholes along the Dead Sea coastline. Geophys. Res. Lett. 42 (20):8383–8390. https://doi.org/10.1002/2015GL066053.

Beck, B.F., 1984. Sinkholes: their geology, engineering and environmental impact. Proceedings of the First Multidisciplinary Conferente on Smkholes/Orlando/Florida, p. 117.

Beck, B.F., 2002. The Karst conferences, consulting reports as science, and geophysical pitfalls. Eng. Geol. 65 (2):81–83. https://doi.org/10.1016/S0013-7952(01)00115-6.

Belfer, I., Bruner, I., Keydar, S., Kravtsov, A., Landa, E., 1998. Detection of shallow objects using refracted and diffracted seismic waves. J. Appl. Geophys. 38 (3):155–168. https://doi.org/10.1016/S0926-9851(97)00025-6 (January).

Berardino, P., Fornaro, G., Lanari, R., Sansosti, E., 2002. A new algorithm for surface deformation monitoring based on small baseline differential SAR interferograms. IEEE Trans. Geosci. Remote Sens. 40 (11):2375–2383. https://doi.org/10.1109/tgrs.2002.803792.

Carbonel, D., Rodríguez-Tribaldos, V., Gutiérrez, F., Galve, J.P., Guerrero, J., Zarroca, M., Roqué, C., Linares, R., McCalpin, J.P., Acosta, E., 2014. Investigating a damaging buried sinkhole cluster in an urban area (Zaragoza city, NE Spain) integrating multiple techniques: geomorphological surveys, DInSAR, DEMs, GPR, ERT, and trenching. Geomorphology 229:3–16. https://doi.org/10.1016/j.geomorph.2014.02.007.

Castellazzi, P., Arroyo-Domínguez, N., Martel, R., Calderhead, A.I., Normand, J.C.L., Gárfias, J., Rivera, A., 2016. Land subsidence in major cities of Central Mexico: interpreting InSAR-derived land subsidence mapping with hydrogeological data. Int. J. Appl. Earth Obs. Geoinf. 47:102–111. https://doi.org/10.1016/j.jag.2015.12.002.

Castellazzi, P., Garfias, J., Martel, R., Brouard, C., Rivera, A., 2017. InSAR to support sustainable urbanization over compacting aquifers: the case of Toluca Valley, Mexico. Int. J. Appl. Earth Obs. Geoinf. 63 (Supplement C):33–44. https://doi.org/10.1016/j.jag.2017.06.011.

Chalikakis, K., Plagnes, V., Guerin, R., Valois, R., Bosch, F.P., 2011. Contribution of geophysical methods to karst-system exploration: an overview. Hydrogeol. J. 19 (6): 1169–1180. https://doi.org/10.1007/s10040-011-0746-x.

Cooper, A.H., Calow, R., 1998. Avoiding Gypsum Geohazards: Guidance for Planning and Construction.

Crosetto, M., Monserrat, O., Cuevas-González, M., Devanthéry, N., Crippa, B., 2016. Persistent Scatterer interferometry: a review. ISPRS J. Photogramm. Remote Sens. 115: 78–89. https://doi.org/10.1016/j.isprsjprs.2015.10.011.

Davis, S.N., Campbell, D.J., Bentley, H.W., Flynn, T.J., 1985. Ground Water Tracers. National ground water association (200pp).

Del Prete, S., Iovine, G., Parise, M., Santo, A., 2010. Origin and distribution of different types of sinkholes in the plain areas of Southern Italy. Geodin. Acta 23 (1–3):113–127. https://doi.org/10.3166/ga.23.113-127.

Di Fiore, Vincenzo, Angelino, Antimo, Passaro, Salvatore, Bonanno, Angelo, 2013. High resolution seismic reflection methods to detect near surface tuff-cavities: a case study in the Neapolitan area, Italy. J. Cave Karst Stud. 1 (April 20):51–59. https://doi.org/10.4311/2011ES0248.

Ferretti, A., Prati, C., Rocca, F., 2001. Permanent scatterers in SAR interferometry. IEEE Trans. Geosci. Remote Sens. 39 (1):8–20. https://doi.org/10.1109/36.898661.

Ford, D., Williams, P.D., 2013. Karst Hydrogeology and Geomorphology. John Wiley & Sons.

Galvão, P., Halihan, T., Hirata, R., 2015. Evaluating karst geotechnical risk in the urbanized area of Sete Lagoas, Minas Gerais, Brazil. Hydrogeol. J. 23 (7):1499–1513. https://doi.org/10.1007/s10040-015-1266-x.

Galve, J.P., Castañeda, C., Gutiérrez, F., Herrera, G., 2015. Assessing sinkhole activity in the Ebro Valley mantled evaporite karst using advanced DInSAR. Geomorphology 229: 30–44. https://doi.org/10.1016/j.geomorph.2014.07.035.

Goldscheider, N., Meiman, J., Pronk, M., Smart, C., 2008. Tracer tests in karst hydrogeology and speleology. Int. J. Speleol. 37 (1), 3.

Gutiérrez, F., Galve, J.P., Lucha, P., Castañeda, C., Bonachea, J., Guerrero, J., 2011. Integrating geomorphological mapping, trenching, InSAR and GPR for the identification and characterization of sinkholes: a review and application in the mantled evaporite karst of the Ebro Valley (NE Spain). Geomorphology 134 (1–2):144–156. https://doi.org/10.1016/j.geomorph.2011.01.018.

Hoover, R., 2003. Geophysical choices for karst investigation. 9ème Conference on Sinkhole and Engineering and Environmental Impacts of Karsts.

Intrieri, E., Gigli, G., Nocentini, M., Lombardi, L., Mugnai, F., Fidolini, F., Casagli, N., 2015. Sinkhole monitoring and early warning: an experimental and successful GB-InSAR application. Geomorphology 241:304–314. https://doi.org/10.1016/j.geomorph.2015.04.018.

Kass, W., Behrens, H., 1998. Tracing Technique in Geohydrology. Balkema.

Krawczyk, C.M., Polom, U., Beilecke, T., 2013. Shear-wave reflection seismics as a valuable tool for near-surface applications. Lead. Edge https://doi.org/10.1190/tle32030256.1 (March).

Lollino, G., Giordan, D., Crosta, G.B., Corominas, J., Azzam, R., Wasowski, J., Sciarra, N., 2015. Engineering Geology for Society and Territory. Vol. 2. Springer.

Marsh-McBirney Inc, 1994. Open channel profiling handbook. 4539 Metropolitan Court, Frederick, Maryland, pp. 21704–29452.

Martel, R., Trépanier, L., Castellazzi, P., Calderhead, A., Deschênes-Rancourt, C., Lévesque, R., 2016. Étude des grottes de Courville à partir de méthodes quantitatives en sciences de la terre: phase II. Québec. Institut national de la recherche scientifique, Centre Eau Terre Environnement (258 pages. Research report 1642).

Massonnet, D., Feigl, K.L., 1998. Radar interferometry and its application to changes in the Earth's surface. Rev. Geophys. 36 (4):441–500. https://doi.org/10.1029/97RG03139.

MDA, 2016. RADARSAT-2 Product Description. RN-SP-52-1238. Issue 1/13: March 21, 2016.

Moore, R., 2005. Slug injection using salt in solution. Streamline Watershed Manag. Bull. 8 (2), 1–6.

Parker, E.H., 2002. MASW in karst terrain. Implications for Detecting Subsidence Features and Lineaments. Maîtrise en sciences de l'université Athen Georgia, GA, USA.

Rantz, S.E., 1982. Measurement and Computation of Streamflow: Volume 2, Computation of Discharge (USGPO).

dos Reis Júnior, J.A., de Castro, D.L., Casas, A., Himi, M., Lima-Filho, F.P., 2015. ERT and GPR survey of collapsed paleocave systems at the western border of the Potiguar Basin in

northeast Brazil. Near Surf. Geophys. 13 (4):369–381. https://doi.org/10.3997/1873-0604.2015013.
Roth, M.J.S., Mackey, J.R., Nyquist, J.E., 1999. A Case Study of the Use of Multi-Electrode Earth Resistively in Thinly Mantled Karst, Proceedings of the Symposium on the Application of Geophysics to Engineering and Environmental Problems, Oakland, California, March 14–18, 1999. :pp. 293–302 https://doi.org/10.4133/1.2922619.
Rubin, Y., Hubbard, S., 2005. Hydrogeophysics. Springer, New York (354 pp).
Rucker, M.L., Panda, B.B., Meyers, R.A., Lommler, J.C., 2013. Using InSAR to detect subsidence at brine wells, sinkhole sites, and mines. Carbonates Evaporites 28 (1–2): 141–147. https://doi.org/10.1007/s13146-013-0134-9.
Speltech, 2013a. L'état des lieux et des connaissances concernant les cavernes de Beauport. Rapport final remis à la Ville de Québec. Speltech Inc., Shefford, Québec.
Speltech, 2013b. La caverne de Beauport située entre le 89 Sylvio et le 76 Brideau - Caractérisation topographique et géomorphologique des vides souterrains établie d'après les relevés de 1997 et confirmée par les observations de 2012. Document remis à la Ville de Québec. Speltech Inc., Shefford, Québec.
Speltech, 2014. Inspection visuelle d'une partie des cavernes situées sous les rues des pionniers et Larue. Rapport final remis à la Ville de Québec. Speltech Inc., Shefford, Québec.
Stockwell, J.W., 1999. The CWP/SU: seismic Unix package. Comput. Geosci. 25 (4): 415–419. https://doi.org/10.1016/s0098-3004(98)00145-9.
Tarantola, A., 1984. Linearized inversion of seismic reflection data. Geophys. Prospect. 32, 998–1015.
Waltham, A.C., Bell, F., Culshaw, M., 2005. Sinkholes and Subsidence: Karst and Cavernous Rocks in Engineering and Construction. Springer, Berlin (382 p).
Yerro, A., Corominas, J., Monells, D., Mallorquí, J.J., 2014. Analysis of the evolution of ground movements in a low densely urban area by means of DInSAR technique. Eng. Geol. 170:52–65. https://doi.org/10.1016/j.enggeo.2013.12.002.
Zini, L., Calligaris, C., Forte, E., Petronio, L., Zavagno, E., Boccali, C., Cucchi, F., 2015. A multidisciplinary approach in sinkhole analysis: the Quinis village case study (NE-Italy). Eng. Geol. 197:132–144. https://doi.org/10.1016/j.enggeo.2015.07.004.